Research Square

Preprints are preliminary reports that have not undergone peer review.
They should not be considered conclusive, used to inform clinical practice,
or referenced by the media as validated information.

Transient Potential Amplification in Dynamically Operated Electrochemical Systems

Xin Xiao

xinxiao@zju.edu.cn

Zhejiang University https://orcid.org/0000-0003-1098-9484

Huili Zeng

Zhejiang University

Zijian Wang

Zhejiang University

Chenglong Gao

Tongji University

Yeyin Li

Zhejiang University

Hongwei Liu

Zhejiang University

Menghao Yang

Shanghai Jiao Tong University

Rong Xu

Xi'an Jiaotong University https://orcid.org/0000-0002-3694-595X

Weilai Yu

University of Toronto https://orcid.org/0000-0002-9420-0702

Baoliang Chen

Zhejiang University https://orcid.org/0000-0001-8196-081X

Physical Sciences - Article

Keywords:

Posted Date: March 30th, 2026

DOI: https://doi.org/10.21203/rs.3.rs-9076047/v1

License: This work is licensed under a Creative Commons Attribution 4.0 International License.
Read Full License

Additional Declarations: There is **NO** Competing Interest.

Transient Potential Amplification in Dynamically Operated Electrochemical Systems

Huili Zeng[1, 2 ,4], Zijian Wang[1, 2, 4], Chenglong Gao[6], Yeyin Li[1, 2, 4], Hongwei Liu[1, 2, 4], Menghao Yang[5], Rong Xu[7], Weilai Yu[8*], Baoliang Chen [1, 2, 3, 4*], Xin Xiao[1, 2, 3, 4 *]

[1] State Key Laboratory of Soil Pollution Control and Safety, Zhejiang University, Hangzhou, Zhejiang 310058, China

[2] Department of Environmental Science, Zhejiang University, Hangzhou, Zhejiang 310058, China

[3] Future Environment Laboratory, Innovation Center of Yangtze River Delta, Zhejiang University, Jiaxing 314100, China.

[4] Zhejiang Provincial Key Laboratory of Organic Pollution Process and Control, Hangzhou, Zhejiang 310058, China

[5] College of Smart Energy, Shanghai Jiao Tong University, Shanghai 200240, China

[6] Shanghai Key Lab. of D&A for Metal Functional Materials, School of Materials Science & Engineering, Tongji University, Shanghai 201804, China

[7] Department of Engineering Mechanics, School of Aerospace Engineering, Xi'an Jiaotong University, Xi'an 710049, China

[8] Department of Chemical Engineering and Applied Chemistry, University of Toronto, Toronto, Ontario ON M5S 3E5, Canada

*Corresponding Author: Prof. & Dr. Xin Xiao, Prof. & Dr. Baoliang Chen, Prof. & Dr. Weilai Yu

(Telephone & Fax: +86-571-8820-6951, E-mail: xinxiao@zju.edu.cn, blchen@zju.edu.cn, weilai.yu@utoronto.ca)

Abstract

Electrochemical technologies underpin hundreds of billions of dollars in industrial value and are increasingly operated under dynamic voltage switching in systems ranging from flow batteries to continuous electrolyzers. Yet the true electrode energetics during such operation remain largely unresolved because absolute potentials are poorly understood in two-electrode devices. Here we resolve electrode potentials operando using a reference-assisted five-channel method and uncover an alternating-current-driven potential excursion (APEX), a transient amplification of electrode potential that can exceed the steady-state value by up to threefold and reach 4.2 V versus the standard hydrogen electrode. We show that APEX arises from spatiotemporal coupling between voltage switching, electrolyte flow and electric-double-layer dynamics, which transiently accesses otherwise inaccessible electrochemical reaction regimes. In a flow-through electrochemical reactor, this phenomenon enables rapid and sustained mineralization of diverse organic chemicals under mild operating voltages with long-term mineralization rate stability (>80%) exceeding 500 h. Our findings reveal a hidden energetic dimension in dynamically operated electrochemical systems and provide a framework for interpreting and designing voltage-switching electrochemical technologies.

Main

Electrochemical technologies underpin hundreds of billions of dollars in global industrial activity, including chlor-alkali production[1,2], electrolytic metallurgy[3-5], organic synthesis[6,7], and rapidly expanding electrochemical energy systems such as batteries and electrolyzers[8-10]. Increasingly, these technologies operate under dynamic conditions in which the applied voltage is periodically switched. Such operation may arise intrinsically, as in battery cycling[11,12] and load-following electrolyzers[13], or be deliberately engineered through pulsed or alternating electrolysis to control interfacial microenvironments, enhance transport[14,15] and improve selectivity[16-18] and durability[19-21]. Despite the growing prevalence of dynamic electrochemical operation, the true electrode energetics under voltage switching remain poorly understood.

A central quantity governing electrochemical reactivity is the absolute electrode potential, which determines which interfacial reactions are thermodynamically accessible and when competing processes such as corrosion, gas evolution or over-oxidation occur[22]. In practical systems, however, electrochemical devices are typically operated in two-electrode configurations, where the applied cell voltage reflects the combined contributions of ohmic losses, polarization and interfacial kinetics. Consequently, the terminal voltage does not uniquely specify the instantaneous interfacial state of either electrode. This ambiguity becomes particularly severe in continuous-flow electrochemical reactors, where strong spatial and temporal gradients in conductivity, pH, gas holdup and polarization can make electrode potentials intrinsically dynamic[14,23-25]. Moreover, most mechanistic studies of voltage switching are performed in three-electrode laboratory cells under reference-controlled potentials[26,27], whereas industrial electrochemical systems generally operate under two-electrode voltage control and strong convection[28-30]. As a result, it remains difficult to identify the true reaction windows, quantify hidden energetic penalties, or translate laboratory insights into predictive design rules for the two electrode configurations that matter most for scale up.

Here we address this challenge by resolving electrode absolute potentials operando in a dynamically operated two-electrode flow reactor. Using a reference-assisted five-channel diagnostic configuration, we discover an alternating-current-driven potential excursion (APEX) (Fig. 1a)-a transient amplification of electrode potential that remains

invisible in the terminal cell voltage yet fundamentally alters accessible electrochemical reaction regimes. The excursion transiently amplifies the electrode potential to values up to three times higher than the steady-state level, reaching 4.2 V versus the standard hydrogen electrode. This hidden energetic regime enables reaction pathways that are inaccessible under constant bias, including deep mineralization of phenol and other persistent organic molecules (Supplementary Fig. 1). Mechanistically, we show that APEX arises from spatiotemporal coupling between voltage-switching timescales, electrolyte transport and electric-double-layer dynamics. Similar behavior is observed across multiple electrode materials, electrolytes and reactor configurations (Fig. 1a, Supplementary Fig. 2), indicating that APEX represents a general phenomenon in dynamically operated electrochemical systems. These findings reveal a previously unrecognized energetic dimension in voltage-switching electrochemistry and provide a framework for interpreting and designing dynamic electrochemical technologies.

Alternating voltage switching enables deep mineralization

To demonstrate the functional significance of the APEX event, we investigated electrooxidation of organic contaminants in a flow-through electrode system (FES) (Fig. 1b, Supplementary Fig. 3), a scalable and industry-relevant architecture that sustains inflow and outflow pH (Supplementary Fig. 4) and minimizes concentration polarization through strong convection[31]. Carbon felt was chosen as the electrode platform because carbon materials uniquely combine chemical robustness, electrical conductivity, and scalable manufacturability under aqueous operation[24,32]. The electrode distance was kept below 110 μm, yielding a low resistance (~1.5 Ω), far lower than that of conventional cells (H-cell, 8.5 Ω; single-chamber cell, 12.2 Ω) (Supplementary Fig. 5). At 3 V cell voltage, phenol and several antibiotics (enrofloxacin, ciprofloxacin, tetracycline hydrochloride, and sulfadiazine) were rapidly removed (Supplementary Fig. 6), yet constant-voltage operation mineralized only ~20-30% to CO_2, whereas periodic switching at 0.01 Hz boosted total organic carbon (TOC) removal to >70% (Supplementary Fig. 1, Supplementary Note 4, Supplementary Figs. 8-13), delivering exceptionally fast and deep phenol mineralization relative to conventional chemical oxidation methods (Supplementary Fig. 14). Periodic switching also markedly enhanced durability, maintaining >80% TOC removal for over 500 h versus <24 h lifetime and much lower TOC removal without switching (Fig. 1c),

consistent with SEM evidence of a clean, structurally intact carbon felt surface after 500 h (Supplementary Fig. 15).

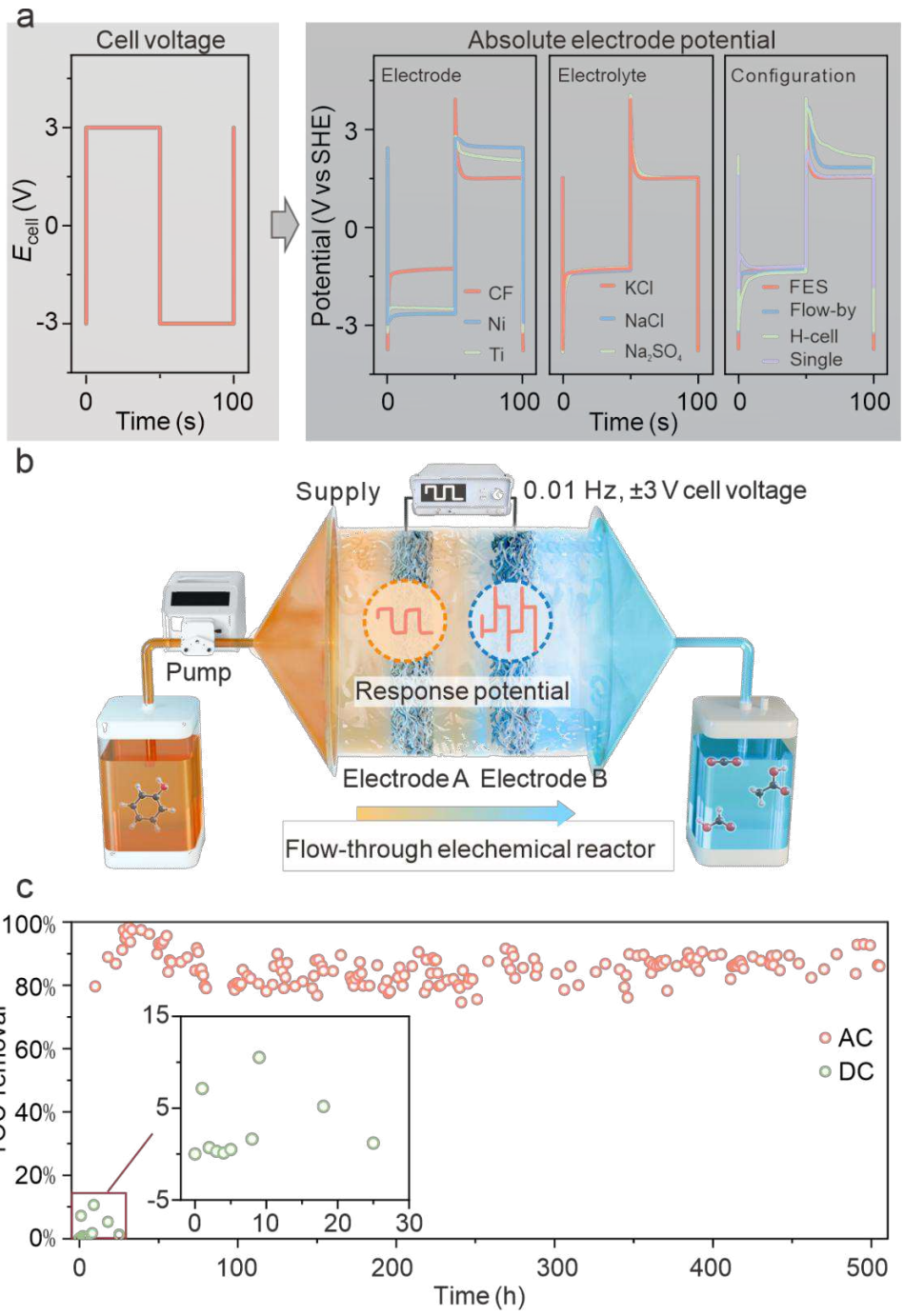


Fig.1| APEX observation and its enabled deep mineralization in a flow-through electrochemical reactor. a, The applied cell voltage and corresponding absolute electrode potential at varied electrode materials, varied electrolytes, varied electrolyzers configurations. **b**. Schematic of FES system. **c**, Long-term evaluation of FES under alternative-current (AC) and direct-current (DC) (Condition: FES, CF electrode, 0.1 mol L^{-1} KCl + 10 mg L^{-1} Phenol). AC condition (orange point), square wave (Supplementary Fig. 9), ±3 V cell voltage, 0.01 Hz, 50% duty cycle; DC condition (green point), constant voltage at 3 V.

Operando resolution of absolute electrode potentials

To elucidate the mechanism by which AC enhances the mineralization of organic chemicals, we first established that the process is dominated by direct interfacial charge transfer, as the measured concentrations of reactive radical species were negligible (Supplementary Figs. 16-18). We focused subsequent mechanistic analysis on phenol because it is produced at massive scale (>12 Mt yr^{-1})[33] underpinned the first fully synthetic plastic (Bakelite)[34] and is regulated as a priority organic pollutant in multiple jurisdictions[35-37]. Beyond the conventional two-channel control of the dual electrodes in the FES, we implemented three additional measurement channels by incorporating an Ag/AgCl reference electrode, yielding a five-channel, reference-assisted configuration (Supplementary Fig. 20). This platform enables simultaneous, real-time resolution of the absolute potentials of each electrode under an imposed cell voltage, thereby quantifying electrode energetics and the associated energy input in an industrially relevant manner. Cell-voltage scans revealed two distinct regimes in the absolute-potential response: capacitive charging and faradaic reaction (Supplementary Fig. 21). When combined with the thermodynamic potentials of water decomposition and organic chemical oxidation (Supplementary Figs. 22-23), an optimal operating cell voltages (3 V) can be rational selected to minimize energy consumption while maintaining high chemical conversion (Supplementary Fig. 24).

Upon applying periodic cell voltage switching, we observed a pronounced alternative current (AC)-driven potential excursion (APEX) at the outflow electrode (E_B), reaching up to 4.2 V vs SHE (Fig. 2a); in contrast, such excursions were absent (or minimal) under direct current (DC) operation at either electrode (Fig. 2a). Remarkably, this APEX peak exceeds the electrochemical stability window of water and, to our knowledge, is captured here for the first time in this architecture. This voltage amplification transiently accesses highly energetic interfacial states that are not achievable under steady DC bias, providing a plausible basis for the observed efficient mineralization. APEX persisted across different duty cycles (Supplementary Fig. 25) and different cell voltages (Supplementary Fig. 26), but emerged only at low switching frequencies (<1 Hz) and vanished at higher frequencies (≥1 Hz) (Supplementary Fig. 27). The loss of APEX at higher switching frequencies closely parallels the decline in phenol mineralization with increasing frequency (Supplementary Fig. 9), supporting a

direct connection between APEX and deep mineralization and providing a mechanistic rationale for the limited mineralization reported under high-frequency AC operation in earlier studies[38-40].

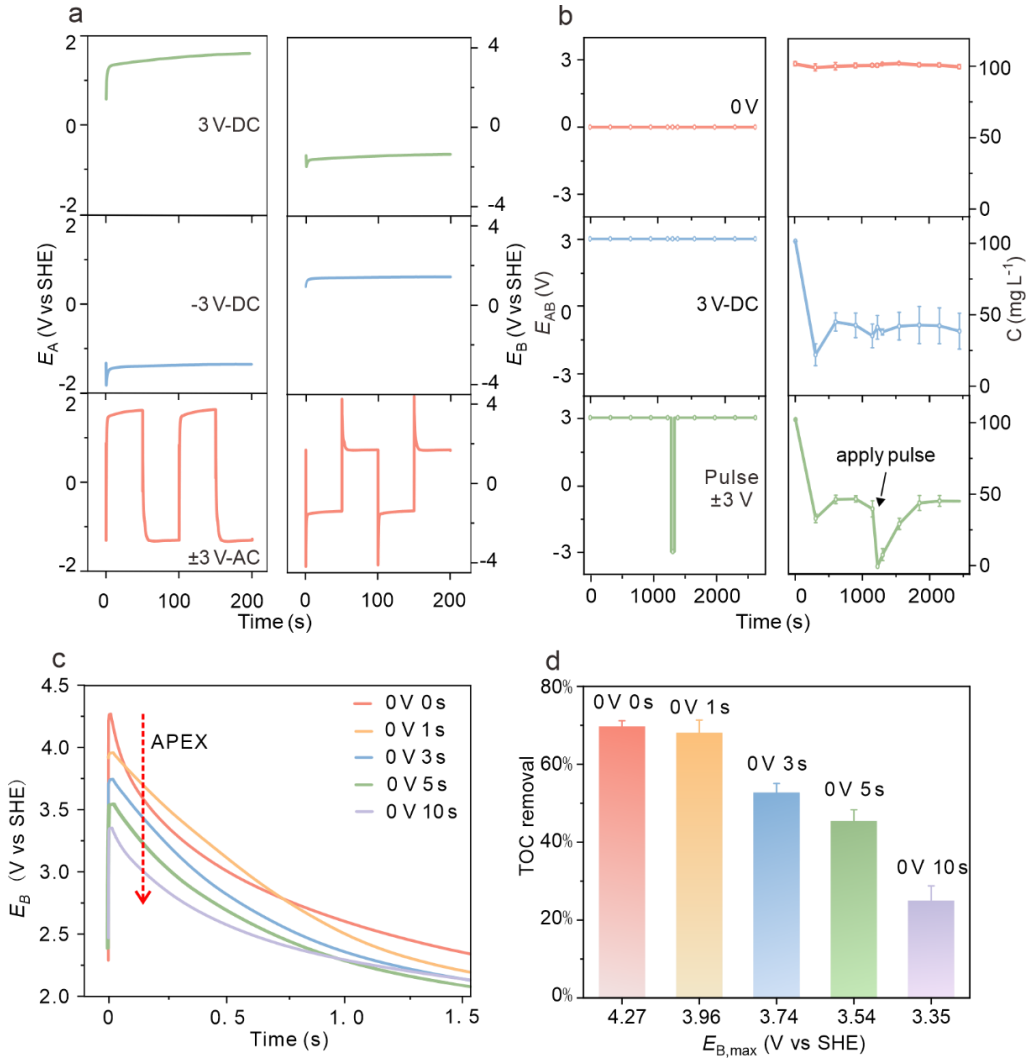


Fig. 2 | Absolute-potential resolution links APEX to deep phenol mineralization. a, The corresponding potentials of electrode A and B under DC and AC. **b**, Experimental setup for validating AC-enhanced phenol removal. **c-d**, The potential of B electrode under different short-circuit durations and corresponding TOC removal. E_A: The absolute potential of inflow electrode (electrode A); E_B: The absolute potential of outflow electrode (electrode B).

APEX drives deep mineralization

To test whether APEX drives the enhanced phenol mineralization, we superimposed a single voltage pulse onto a DC baseline (Fig. 2b). At 0 V, the effluent phenol concentration matched the influent (100 mg L^{-1}), whereas a constant 3 V reduced it to ~50 mg L^{-1}. Strikingly, introducing a brief ±3 V pulse (duration: 50 s) caused the

phenol concentration to drop to near-zero, then gradually relaxing back to the steady ~50 mg L^{-1} level, directly implicating switching-induced APEX as the origin of the transient, high-efficiency mineralization. If deep mineralization is indeed governed by APEX, its amplitude should be decisive. We therefore implemented a programmable short-circuit step to modulate the APEX peak (Supplementary Fig. 28). As shown in Fig. 2c, d, tuning the shorting duration systematically lowered the APEX peak height from 4.27 to 3.35 V (vs SHE), accompanied by a pronounced drop in phenol mineralization from ~70% to ~20%. Consistent with this interpretation, reducing the nominal cell voltage to 1.0 and 1.5 V still delivered ~50% and ~71% mineralization, respectively (Supplementary Fig. 29), because APEX persisted under these conditions (Supplementary Fig. 26); in contrast, constant-voltage operation over 1-3 V consistently yielded <20% mineralization. Collectively, these results establish APEX as the operative driver of deep phenol mineralization, with the APEX peak height acting as a key control parameter.

Spatiotemporal coupling governs APEX-enhanced mineralization

To explain the emergence of the APEX peak, we propose a spatiotemporal coupling mechanism in which APEX arises from matching a temporal scale set by the switching frequency with a spatial/transport scale governed by electrolyte flow. In this framework, both frequency and flow can independently modulate the APEX event (Supplementary Fig. 27), whereas their proper coupling further promotes deep phenol mineralization. Because APEX reflects the absolute electrode potential, it is highly sensitive to interfacial factors that regulate the electrochemical double layer (EDL)[41-43], particularly the local electrolyte composition near the surface (e.g., pH). When the instantaneous absolute potential extends beyond the water-stability window, the near-electrode microenvironment becomes non-uniform and can develop pronounced pH gradients, as directly visualized by photograph recording (Supplementary Fig. 30). Such spatially heterogeneous pH fields are consistent with, and likely contribute to the APEX peaks.

Flow-through operation further reshapes this interfacial response. Convection can compress the EDL, facilitating charge/species exchange at the interface (Supplementary Fig. 31)[44] (Supplementary Fig. 32)[45], as supported by changes in the distribution of relaxation times (DRT) spectrum (Supplementary Fig. 33). We therefore

hypothesized that frequency-flow coupling governs how pH gradients build up and relax during voltage-switching cycles. To test this, COMSOL software was used to simulate pH distributions along the dual electrodes as a function of switching duration under different flow rates and frequencies (Fig. 3a-b, Supplementary Fig. 34). Interestingly, the simulated pH patterns are disorganized for 0 $mL \cdot min^{-1}$@0.01 Hz, 0.2 $mL \cdot min^{-1}$@0.01 Hz, 1 $mL \cdot min^{-1}$@0.1 Hz and 1 $mL \cdot min^{-1}$@1 Hz, suggesting weak or absent coupling between flow and frequency (Fig. 3a-b, Supplementary Fig. 33). In contrast, when 0.01 Hz is paired with 1 mL min^{-1}, the pH field evolves into an ordered, ladder-like profile across cycles, ensuring that at any given moment the inflow and outflow electrodes experience distinct pH environments. If the flow is further increased, the pH pattern remains ordered but the pH contrast between inflow and outflow diminishes, which is unfavorable for phenol mineralization (Supplementary Fig. 32). Collectively, these results indicate that efficient APEX-driven mineralization requires matched frequency-flow coupling to establish and sustain pH gradients throughout voltage-switching cycles.

Electric-double-layer origin of APEX

To gain mechanistic insight into APEX, we analyzed how voltage switching reshapes the EDL, which directly governs the instantaneous absolute potential (Fig. 3c). The process can be rationalized in three consecutive stages. (**Stage I)**. When +3 V is applied to electrode A (the inflow electrode; absolute potential ~1.5 V vs SHE), water splitting acidifies the local environment and enriches the EDL at electrode A with anions (e.g., Cl^-). Meanwhile, the generated H^+ is convected downstream toward electrode B, where the interfacial region becomes enriched with densely packed cations (H^+ together with K^+). This cation accumulation increases the local Nernst potential and strengthens the interfacial electric field at electrode B. **(Stage II)**. Upon abruptly reversing the cell voltage to -3 V, electron transfer in the electrode backbone responds far faster than ion migration within the EDL. As a result, the interfacial ionic configuration momentarily lags behind the polarity reversal, producing a transient "potential superposition" state: cations remain crowded near the interface while the electrode substrate has switched to positively charged (stage II at electrode B in Fig. 3c). This mismatch generates a pronounced transient excursion in the absolute potential of electrode B, manifested as the APEX event. **(Stage III)**. Subsequently, double-layer

discharge drives redistribution of interfacial ions away from the surface, and the absolute potential relaxes back to a steady value. In the subsequent half-cycle, OH^- becomes the dominant interfacial species, giving rise to an opposite voltage excursion.

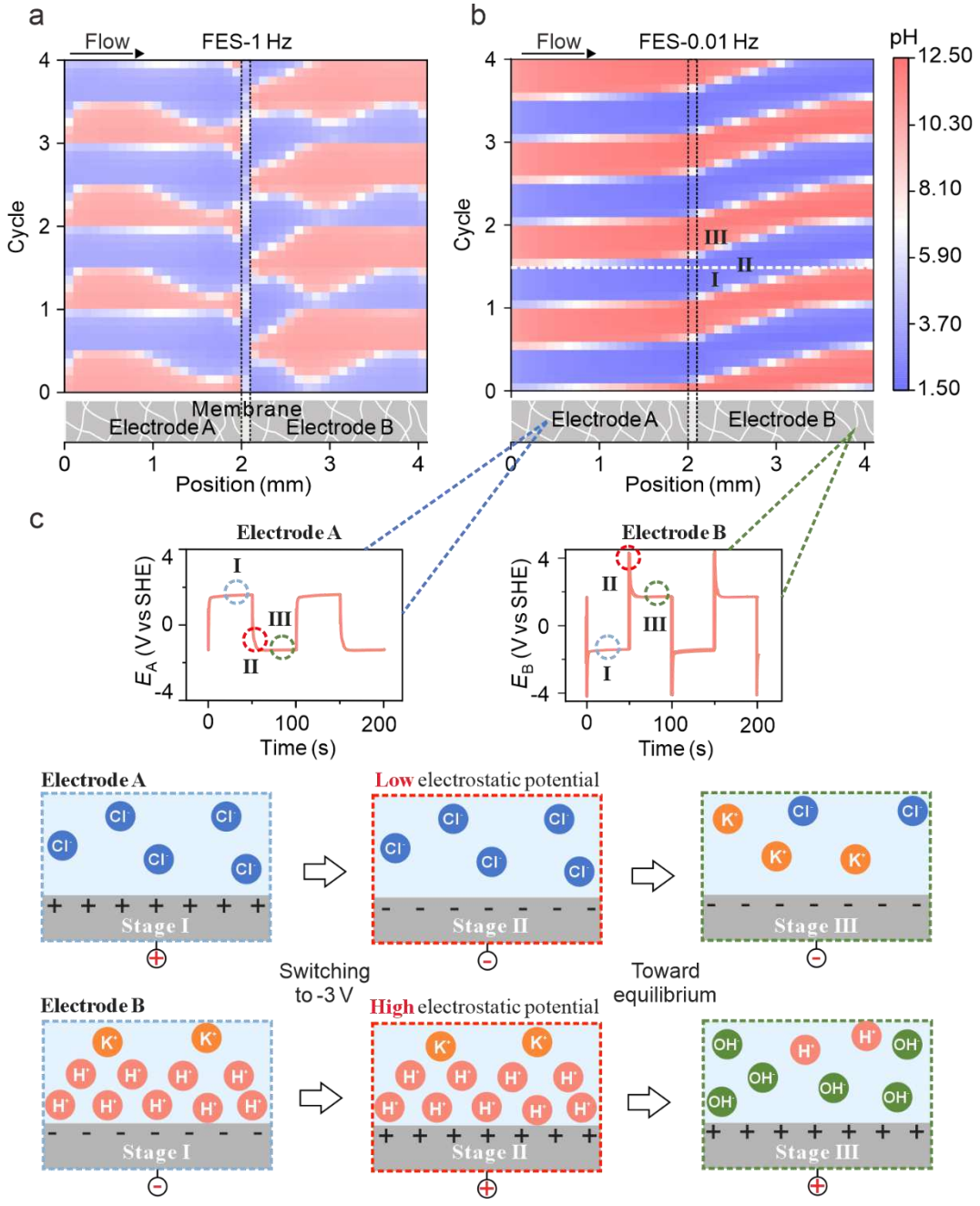


Fig. 3 | Spatiotemporal and electric-double-layer origins of APEX. a-b, pH distribution at different AC frequencies in FES simulated by COMSOL (flow rate: 1 mL min^{-1}). **c**, Schematic representation of the effects of the electrode interfacial microenvironment[46-48].

This framework also explains why APEX is not observed at electrode **A** (the inflow electrode). Protons and hydroxide ions exhibit faster interfacial charge-transfer[49] and higher ionic mobility than K^+ or Cl^-[22], and electrode A is continuously refreshed by incoming electrolyte, which suppresses interfacial accumulation of H^+/OH^- and thus limits transient potential build-up. The role of EDL dynamics in enabling APEX-assisted mineralization is further supported by control experiments in the single-chamber cell (Supplementary Figs. 36-37): although it has comparable EDL capacitance, it exhibits only minor voltage spikes and correspondingly modest enhancement in phenol mineralization under AC operation because of the lack of H^+/OH^- downstream convection compare to FES. Finally, tuning the initial electrolyte pH provides controllable height and sharpness in the APEX peak (Supplementary Fig. 38), consistent with our hypothesis and highlighting the coupled roles of switching frequency and the local pH microenvironment in governing EDL charging/discharging.

Operando Raman captures APEX-driven surface chemistry

We using shell-isolated nanoparticle-enhanced Raman spectroscopy (SHINERS)[50] to operando monitor the time-dependent transformation of phenol on both electrodes (Fig. 4, Supplementary Figs. 39-40). According to Raman spectra of standard samples, phenol exhibits characteristic bands at 997 cm^{-1} (aromatic ring) and 1024 cm^{-1} (aromatic C-H stretching)[51]. Its oxidation products also display identifiable spectral features that serve as molecular fingerprints during operando Raman analysis (Supplementary Fig. 41). Control experiments confirm that, in the absence of an applied potential, the Raman signals of phenol remain constant throughout the measurement, demonstrating its stability under SERS testing conditions (Supplementary Fig. 41).

Upon applying an alternating cell voltage at 0.01 Hz, the absolute potential of the inflow electrode (**A**) oscillates between ±1.5 V (vs SHE) without showing APEX event, during which the characteristic peaks of phenol progressively diminish and new peaks corresponding to p-benzoquinone, catechol, and other typical oxidation products emerge (Fig. 4c). These reaction products are consistent with those detected in the effluent under direct-current operation (Supplementary Fig. 10). In contrast, on the outflow electrode (**B**), the Raman spectrum detected at multiple organic chemicals at 0 s, including phenol, p-benzoquinone, catechol, resorcinol that could be flushed from the inflow electrode (**A**) (Fig. 4d). However, at 50 s, when APEX happened on the

outflow electrode (absolute potential reaches up to 4.2 V vs SHE), the characteristic peaks of phenol and its oxidation products rapidly decay or disappear entirely. After one full AC cycle, only the spectral features of the carbon-based electrode material remain, providing a direct visual evidence that the APEX event at outflow electrode (**B**) is responsible for the high mineralization process instead of inflow electrode (**A**), matching well with the above mentioned EDL-driven APEX mechanism.

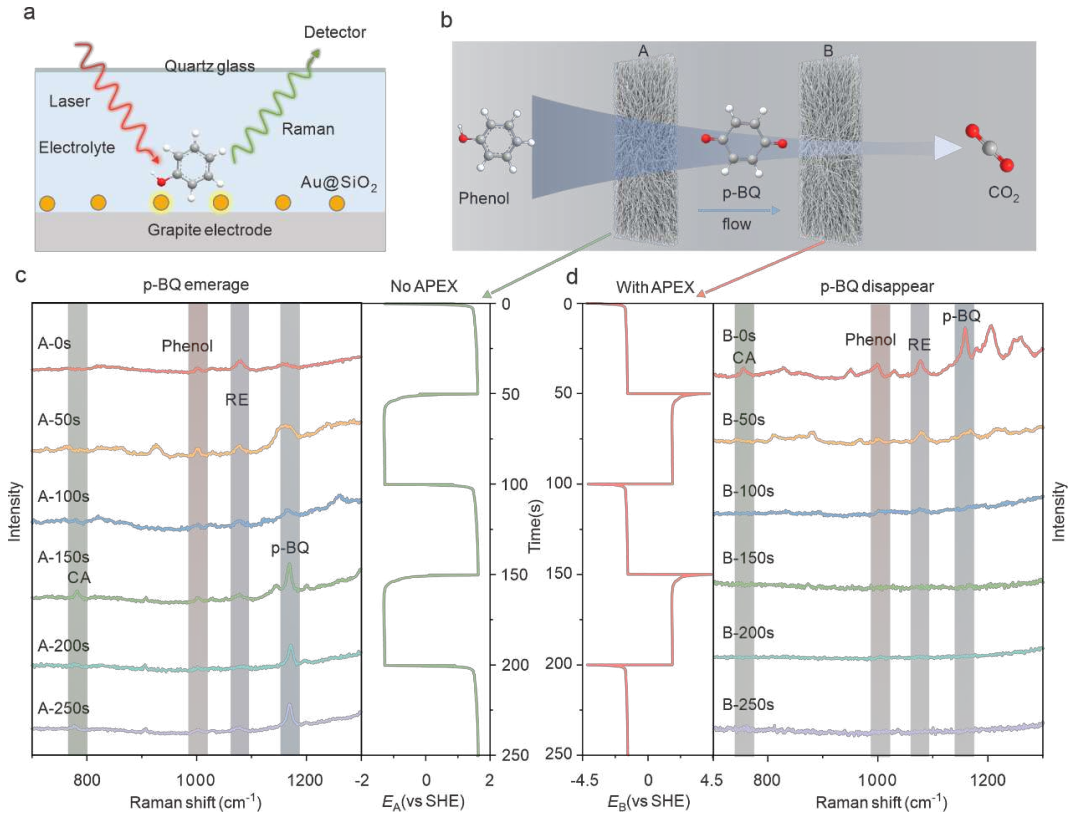


Fig. 4 | Operando electrochemical Raman spectroscopy of phenol under AC condition. a, Schematic illustration of the shell-isolated nanoparticle-enhanced Raman spectroscopy (SHINERS) technique. **b**, Diagram of the reaction process of phenol in two electrodes. **c-d**, The time series of the Raman spectrum and the potential of electrode A (**c**) and electrode B (**d**). CA : catechol；RE: resorcinol；p-BQ: 1,4-benzoquinone.

Molecular basis for APEX-enabled mineralization

Electrochemical measurements and in situ surface enhanced Raman spectra collectively indicate that APEX is decisive for phenol mineralization. To obtain molecular-level insight into this behavior, we use molecular dynamics (MD) simulations to quantify the interaction energy between phenol and carbon electrodes under different potentials, combined with density functional theory (DFT) calculations

to resolve potential-dependent charge redistribution. A constant-potential setup was implemented by constructing a potassium electrode as the reference, a phenol containing electrolyte region in the middle, and a bottom graphite layer serving as the working electrode (Fig. 5a). The phenol-graphite interaction energy decreases monotonically as the potential increases. Notably, when the applied potential exceeds 3.2 V (vs SHE), the interaction energy becomes negative, implying spontaneous adsorption and subsequent interfacial reaction under such high-potential conditions (Fig. 5b).

Bader charge analysis further clarifies the electron-transfer process from a charge-distribution perspective. As shown in Fig. 5b, the net Bader charge transfer between phenol and graphite remains near zero when the absolute potential is below 3.2 V vs SHE, but rises sharply to ~0.15 e- per phenol molecule when the potential increases to 3.7 V vs SHE, evidencing direct charge transfer from phenol to the graphite surface. Differential charge-density map (Fig. 5c) provides a spatial view of this process: blue regions indicate electron depletion and yellow regions indicate electron accumulation. With increasing potential, phenol exhibits progressively stronger electron depletion, consistent with enhanced interfacial electron transfer. In line with the interaction-energy trend, the net charge change of phenol becomes negative once the potential exceeds 3.2 V vs SHE (Fig. 5b), indicating direct electro-oxidation. At 3.7 V vs SHE, pronounced electron redistribution emerges between graphene interlayers, suggesting that high potentials can additionally activate interlayer charge transport. Together, MD simulations and Bader analysis support that elevated potentials facilitate phenol oxidation.

To connect these electronic signatures with chemical outcomes, we quantified more than nine reaction products using liquid chromatography and ion chromatography, including hydroquinone, resorcinol, catechol, 1,4-benzoquinone, formic acid, acetic acid, oxalic acid, malonic acid, and succinic acid (Supplementary Figs. 10, 12). We then proposed 53 one-electron steps for the mineralization pathway from phenol to CO_2 and computed the Gibbs free-energy barrier for each step using Gaussian software (Supplementary Fig. 42). On the basis of these energetics, we identify the rate-limiting step as the oxidation of p-benzoquinone, requiring an effective potential of 5.28 V vs SHE (Fig. 5d). This high-potential bottleneck is consistent with our conclusion that the APEX peak is required for deep phenol mineralization, and it also rationalizes why

product distributions shift between hydroquinone-dominated and p-benzoquinone-dominated regimes under constant-voltage operation (Supplementary Figs. 10, 12), in agreement with many prior oxidation studies reported in the literature[52,53].

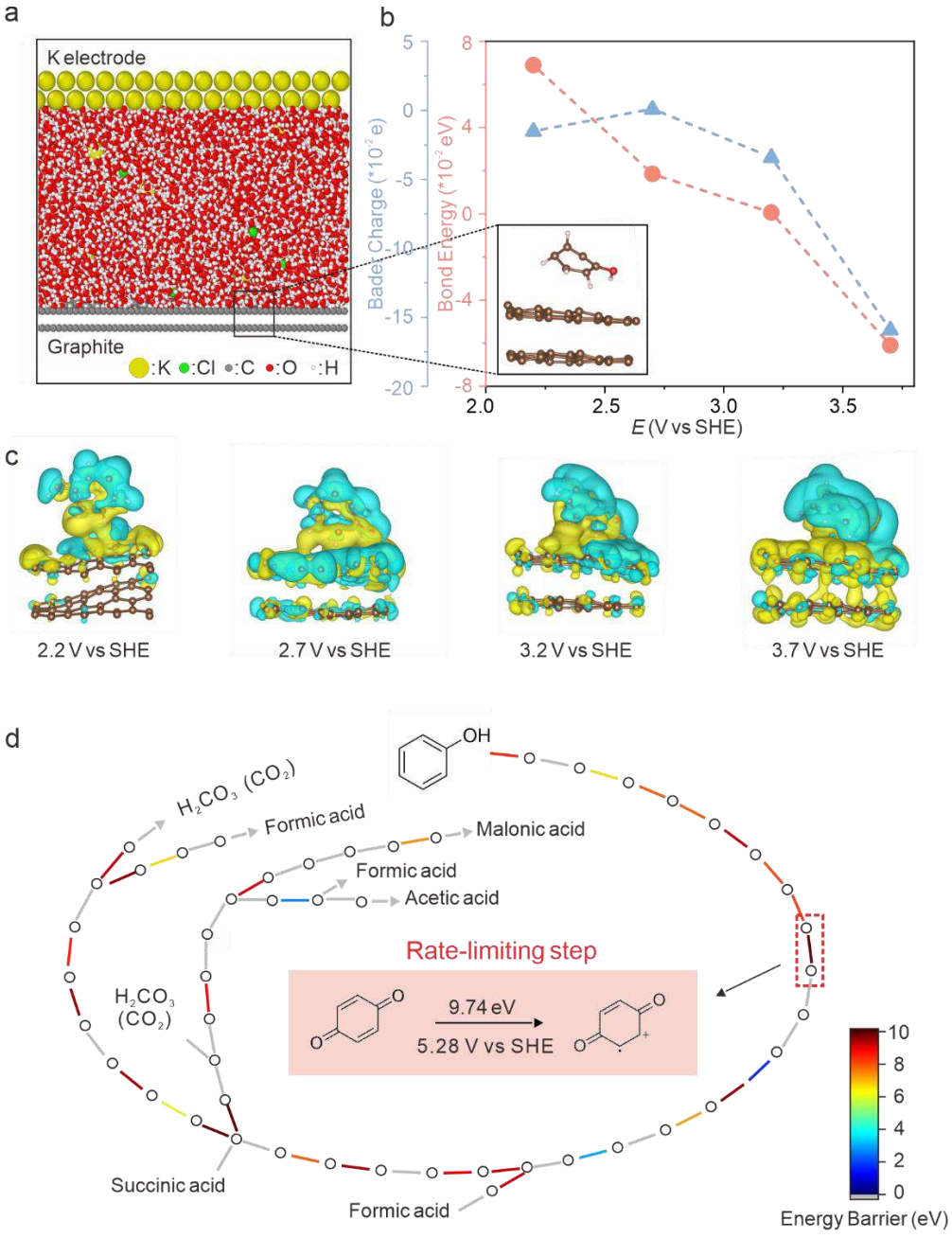


Fig. 5 | Potential-dependent charge transfer and pathways for phenol mineralization. a, A snapshot of the MD model, where yellow spheres represent K atoms or K^+ ions, red for O atoms, white for H atoms, green for Cl^- ions, and grey for C atoms. **b,** Bond energy between phenol and the electrode, along with the Bader charge of phenol, obtained from MD simulations. **c,** Differential charge density distribution for phenol and the electrode, blue and yellow topologies denote electron depletion and accumulation, respectively. The iso-surface value is 0.02 e/Å. **d**, Stepwise reaction energy barriers along the mineralization pathways and key intermediates.

Scalability and techno-economic analysis

Building on these results, we evaluated the system's practical potential by scaling up the reactor and increasing the flow rate to 6 L h^{-1} (Fig. 6a), approaching an industrially relevant throughput. Under continuous operation, the reactor stably treated 450 L of water, achieving complete phenol removal and 60% total organic carbon (TOC) removal, demonstrating rapid and efficient remediation (Fig. 6b). Motivated by this performance, we performed a techno-economic analysis (TEA) to quantify key cost drivers of the FES and benchmark it against established mineralization approaches for organic contaminants, including catalytic ozonation (O_3), the homogeneous Fenton process, and electrochemical Fenton oxidation (EO) (Fig. 6c). Across technologies, we accounted for direct material inputs (e.g., electrodes and reagents), electricity consumption, and any required pre-treatment steps. The analysis shows that treating 1 m^3 of wastewater with our system costs $1.4, substantially lower than the three comparators (Fig. 6d). Notably, electricity accounts for only 1.3% of the total cost, highlighting the energy-efficient advantage of the proposed process.

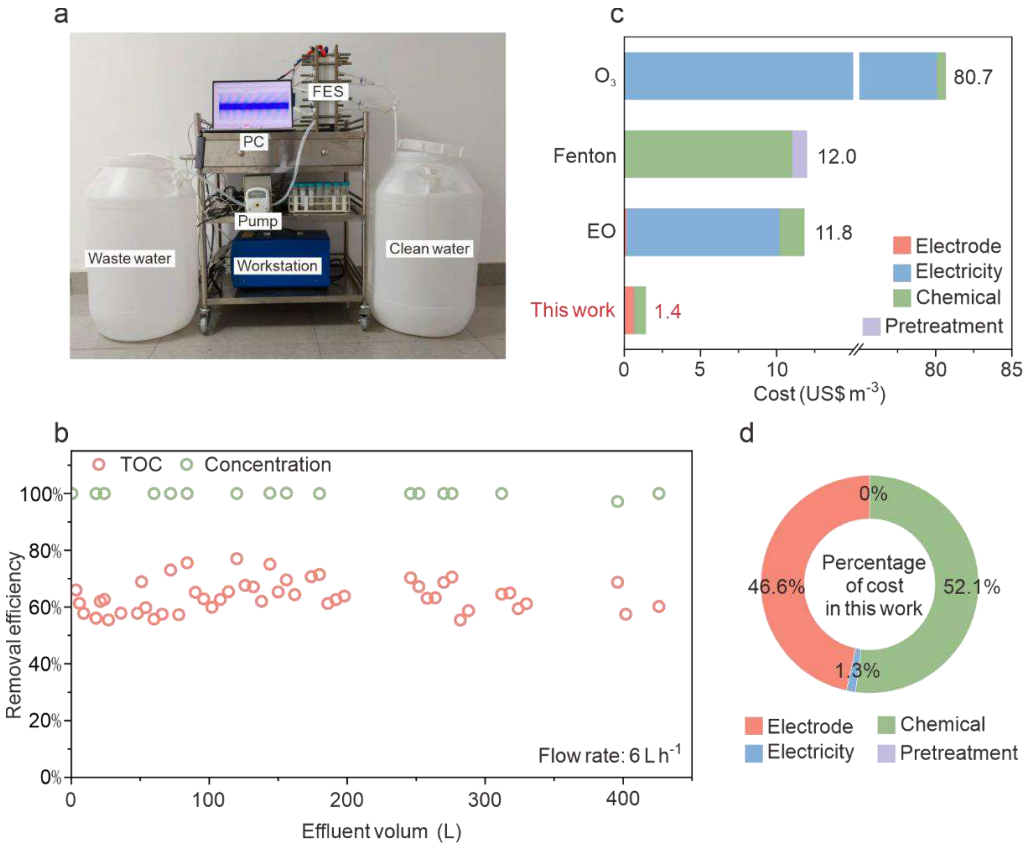


Fig. 6 | Scale-up device and techno-economic analysis. a, The image of the scale up FES. **b**, Simultaneous removal of TOC and phenol of scale up FES (Flow rate: 6 L h^{-1}). **c**, Treatment

costs per cubic meter of wastewater using four different AOP systems (O_3[54], Fenton, E-Fenton, EO[55] and this work). **d**, The proportion of each cost in this system.

Discussion

In summary, we directly resolve absolute electrode potentials operando in a dynamically operated two-electrode flow reactor and uncover an alternating-current-driven potential excursion (APEX) that remains hidden in the terminal cell voltage yet fundamentally alters interfacial electrochemistry. The excursion transiently amplifies electrode potentials far beyond steady-state values, opening access to reaction regimes that are otherwise inaccessible under constant bias. In a flow-through electrochemical reactor, this hidden energetic state enables rapid and sustained mineralization of diverse organic chemicals under comparatively mild operating voltages with long-term TOC removal stability (>80%) exceeding 500 h.

Mechanistically, APEX originates from spatiotemporal coupling between voltage-switching timescales, electrolyte transport and electric-double-layer dynamics, which transiently trap and release ionic charge near the interface. This coupling generates short-lived but highly energetic electrochemical states that cannot be inferred from the applied cell voltage alone. Because dynamic operation is pervasive in electrochemical technologies-from pulsed electrocatalysis to battery cycling and load-following electrolyzers-such transient potential amplification may influence reaction selectivity, degradation pathways and materials evolution in many systems where the apparent operating voltage appears benign.

More broadly, our results reveal a previously unrecognized energetic dimension in dynamically operated electrochemistry. By linking waveform control, transport processes and absolute electrode potentials, the APEX framework provides a diagnostic and design principle for understanding and engineering voltage-switching electrochemical systems, with implications for electrochemical synthesis, environmental remediation and energy conversion technologies.

Reference

1 Lim, H. W., Park, J. H., Yan, B., Kim, J. Y. & Lee, C. W. Liquid-diffusion electrode with core-shell structured mixed metal oxide catalyst for near-zero polarization in chlor-alkali electrolysis. *Appl. Catal., B* **322**, 122095, (2023).

2 MarketsandMarkets. *Chlor-alkali market – size, share & industry forecast to 2026.*, (MarketsandMarkets., 2021) https://www.marketsandmarkets.com/Market-Reports/chlor-alkali-market-708.html.

3 Li, G. *et al.* Nitrous oxide emissions: A long-neglected challenge in the aluminum electrolysis industry. *Environ. Sci. Technol. Lett.* **12**, 799-803, (2025).

4 Lin, B. & Xu, L. Energy conservation of electrolytic aluminum industry in China. *Renew. Sust. Energ. Rev.* **43**, 676-686, (2015).

5 Research, S. *Electroplating market size, share, trend, forecast, competitive analysis, and growth opportunity: 2025–2032*, (Stratview Research, 2025) https://www.stratviewresearch.com/4224/electroplating-market.html.

6 Mathison, R. *et al.* Molecular processes that control organic electrosynthesis in near-electrode microenvironments. *J. Am. Chem. Soc.* **147**, 4296-4307, (2025).

7 Cardoso, D. S. P., Sljukic, B., Santos, D. M. F. & Sequeira, C. A. C. Organic electrosynthesis: From laboratorial practice to industrial applications. *Org. Process Res. Dev.* **21**, 1213-1226, (2017).

8 El-Shafie, M. Hydrogen production by water electrolysis technologies: A review. *Results Eng.* **20**, 101426, (2023).

9 Sha, Q. *et al.* 10,000-h-stable intermittent alkaline seawater electrolysis. *Nature* **639**, 360-367, (2025).

10 Bu, F. *et al.* Electrocatalytic reductive deuteration of arenes and heteroarenes. *Nature* **634**, 592-599, (2024).

11 Liu, F. *et al.* Dynamic spatial progression of isolated lithium during battery operations. *Nature* **600**, 659-663, (2021).

12 Ye, L. *et al.* A rechargeable calcium–oxygen battery that operates at room temperature. *Nature* **626**, 313-318, (2024).

13 Wang, C. R. *et al.* Proton exchange membrane (PEM) water electrolysis: Cell-level considerations for gigawatt-scale deployment. *Chem. Rev.* **125**, 1257-1302, (2025).

14 Hu, Q. *et al.* Pulsed co-electrolysis of carbon dioxide and nitrate for sustainable urea synthesis. *Nat. Sustain.* **7**, 442-451, (2024).

15 Ye, K. *et al.* Molecular level insights on the pulsed electrochemical CO_2 reduction. *Nat. Commun.* **15**, 9781, (2024).

16 Blanco, D. E., Lee, B. & Modestino, M. A. Optimizing organic electrosynthesis through controlled voltage dosing and artificial intelligence. *Proc. Natl. Acad. Sci. U. S. A.* **116**, 17683-17689, (2019).

17 Zhang, Y. *et al.* Oxy-reductive C-N bond formation via pulsed electrolysis. *Nat. Commun.* **16**, 8106, (2025).

18 Chen, W. *et al.* Pulse potential mediated selectivity for the electrocatalytic oxidation of glycerol to glyceric acid. *Nat. Commun.* **15**, 2420, (2024).

19 Timoshenko, J. *et al.* Steering the structure and selectivity of CO_2 electroreduction catalysts by potential pulses. *Nat. Catal.* **5**, 259-267, (2022).

20 Zeng, L. *et al.* Asymmetric-waveform alternating current-promoted silver catalysis for C–H phosphorylation. *Nat. Synth.* **2**, 172-181, (2023).

21 Liu, Y. *et al.* Mitigating $CaCO_3$ crystal nucleation and growth through continuous ion displacement via alternating electric fields. *Nat. Commun.* **16**, 35, (2025).

22 Bard, A. J., Faulkner, L. R. & White, H. S. *Electrochemical methods: Fundamentals and applications*. (Wiley-Blackwell, 2022).

23 Li, S., Fu, X., Nørskov, J. K. & Chorkendorff, I. Towards sustainable metal-mediated ammonia electrosynthesis. *Nat. Energy* **9**, 1344-1349, (2024).

24 Noël, T., Cao, Y. & Laudadio, G. The fundamentals behind the use of flow reactors in electrochemistry. *Accounts Chem. Res.* **52**, 2858-2869, (2019).

25 Cao, Y., Soares, C., Padoin, N. & Noël, T. Gas bubbles have controversial effects on Taylor flow electrochemistry. *Chem. Eng. J.* **406**, 126811, (2021).

26 Casebolt, R., Levine, K., Suntivich, J. & Hanrath, T. Pulse check: Potential opportunities in pulsed electrochemical CO_2 reduction. *Joule* **5**, 1987-2026, (2021).

27 Kim, M., Kim, Y., Lee, G., Ruoff, R. S. & Lee, S. H. Electrochemical functionalization of graphene-on-Cu(111): Reactivity, onset potentials, and mechanistic insights. *Adv. Sci.* **12**, 2501798, (2025).

28 Tanbouza, N., Ollevier, T. & Lam, K. Bridging lab and industry with flow electrochemistry. *iScience* **23**, 101720, (2020).

29 Seidler, J., Strugatchi, J., Gärtner, T. & Waldvogel, S. R. Does electrifying organic synthesis pay off? The energy efficiency of electro-organic conversions. *MRS Energy Sustain.* **7**, 42, (2020).

30 He, F. *et al.* Accelerating net-zero carbon emissions by electrochemical reduction of carbon dioxide. *J. Energy Chem.* **79**, 398-409, (2023).

31 Sun, J. *et al.* Redox flow batteries and their stack-scale flow fields. *Carbon Neutrality* **2**, 30, (2023).

32 Huong Le, T. X., Bechelany, M. & Cretin, M. Carbon felt based-electrodes for energy and environmental applications: A review. *Carbon* **122**, 564-591, (2017).

33 Energy., S. P. G. *Chemical Economics Handbook-Phenol*, (S&P Global Energy, 2025) https://www.spglobal.com/content/dam/spglobal/ci/en/documents/products/pdf/CI_0325_Global_CEH_Phenol_Abstract.pdf.

34 American Chemical Society National Historic Chemical landmarks, *Bakelite: The world's first synthetic plastic.*, (American Chemical Society, 1993) http://www.acs.org/content/acs/en/education/whatischemistry/landmarks/bakelite.html.

35 Ministry of ecology and environment the people's republic of China. *Freshwater Aquatic Organisms Water Quality Criteria Technical Report - Phenol*, (Ministry of ecology and environment the people's republic of China, 2020) https://www.mee.gov.cn/xxgk2018/xxgk/xxgk01/202012/t20201224_814675.html.

36 United States Environmental Protection Agency. *Priority Pollutant List*, (United States Environmental Protection Agency, 2015) https://www.epa.gov/sites/default/files/2015-09/documents/priority-pollutant-list-epa.pdf.

37 Ministry of the Environment, Government of Japan. (Ministry of the Environment, Government of Japan, 2012) https://www.env.go.jp/en/chemi/prtr/substances/list.html.

38 Wang, J., Wang, A., Song, J., Zhang, I. Y. & Huang, R. A sustainable electrochemical strategy utilizing pulsed alternating current and dual carbon felt electrodes for enhanced degradation of organic pollutants: Oxidation performance and mechanisms. *J. Environ. Chem. Eng.* **12**, 112999, (2024).

39 Mu'azu, N. D., Al-Yahya, M., Al-Haj-Ali, A. M. & Abdel-Magid, I. M. Specific energy consumption reduction during pulsed electrochemical oxidation of phenol using graphite electrodes. *J. Environ. Chem. Eng.* **4**, 2477-2486, (2016).

40 Wei, J., Zhu, X. & Ni, J. Electrochemical oxidation of phenol at boron-doped diamond electrode in pulse current mode. *Electrochim. Acta* **56**, 5310-5315, (2011).

41 Pershaanaa, M., Bashir, S., Ramesh, S. & Ramesh, K. Every bite of Supercap: A brief review on construction and enhancement of supercapacitor. *J. Energy Storage* **50**, 104599, (2022).

42 Cheng, Q. & Chen, W. Analysis of the electrolyte characteristics on the performance of electric double layer capacitor. *J. Environ. Chem. Eng.* **469**, 228404, (2020).

43 Favaro, M. *et al.* Unravelling the electrochemical double layer by direct probing of the solid/liquid interface. *Nat. Commun.* **7**, 12695, (2016).

44 Rocha, F. & Proost, J. Discriminating between the effect of pulse width and duty cycle on the hydrogen generation performance of 3-D electrodes during pulsed water electrolysis. *Int. J. Hydrog. Energy* **46**, 28925-28935, (2021).

45 Ni, X.-Y. *et al.* Enhancing disinfection performance of the carbon fiber-based flow-through electrode system (FES) by alternating pulse current (APC) with low-frequency square wave. *Chem. Eng. J.* **410**, 128399, (2021).

46 Guo, J. *et al.* Direct seawater electrolysis by adjusting the local reaction environment of a catalyst. *Nat. Energy* **8**, 264-272, (2023).

47 Singh, M. R., Kwon, Y., Lum, Y., Ager, J. W. & Bell, A. T. Hydrolysis of electrolyte cations enhances the electrochemical reduction of CO_2 over Ag and Cu. *J. Am. Chem. Soc.* **138**, 13006-13012, (2016).

48 Chen, C. *et al.* Local reaction environment in electrocatalysis. *Chem. Soc. Rev.*, (2024).

49 Xu, K. *Electrolytes, Interfaces and Interphases*. (The Royal Society of Chemistry, 2023).

50 Wang, Y.-H. *et al.* In situ Raman spectroscopy reveals the structure and dissociation of interfacial water. *Nature* **600**, 81-85, (2021).

51 Sánchez-Cortés, S. & García-Ramos, J. V. Adsorption and Chemical Modification of Phenols on a Silver Surface. *J. Colloid Interface Sci.* **231**, 98-106, (2000).

52 Zhao, G. *et al.* Fabrication and electrochemical treatment application of a novel lead dioxide anode with superhydrophobic surfaces, high oxygen evolution potential, and oxidation capability. *Environ. Sci. Technol.* **44**, 1754-1759, (2010).

53 Pei, S., You, S. & Zhang, J. Application of pulsed electrochemistry to enhanced water decontamination. *ACS ES&T Eng.* **1**, 1502-1508, (2021).

54 Cañizares, P., Paz, R., Sáez, C. & Rodrigo, M. A. Costs of the electrochemical oxidation of wastewaters: A comparison with ozonation and Fenton oxidation processes. *J. Environ. Manage.* **90**, 410-420, (2009).

55 Chen, K.-Y. *et al.* Biological waste-derived dual-site catalyst empowers electro-fenton systems to sustainably decontaminate livestock wastewater. *ACS ES&T Eng.* **4**, 3057–3066, (2024).

56 Wang, Y.-H. *et al.* In situ electrochemical Raman spectroscopy and ab initio molecular dynamics study of interfacial water on a single-crystal surface. *Nat. Protoc.* **18**, 883-901, (2023).

57 Wan, T. H., Saccoccio, M., Chen, C. & Ciucci, F. Influence of the discretization methods on the distribution of relaxation times deconvolution: Implementing radial basis functions with drttools. *Electrochim. Acta* **184**, 483-499, (2015).

58 Soni, R. *et al.* Lithium-sulfur battery diagnostics through distribution of relaxation times analysis. *Energy Storage Mater.* **51**, 97-107, (2022).

59 Gao, C. *et al.* Interfacial atomistic reactive mechanisms of magnesium batteries. *Energy Storage Mater.* **80**, 104361, (2025).

Methods

Materials

Carbon felt electrodes were purchased from Shanghai Leton Industrial Co., Ltd., China. After cleaning and cutting, they were treated in an oxygen atmosphere at 180 W for 1 min using a plasma cleaner (Osat, Beijing Optoelectronic Technology Co., Ltd., China) prior to use. Ag/AgCl reference electrodes were obtained from Shanghai Chuxi Industrial Co., Ltd., China. Ti and Ni foam electrode were purchased from Dongguan Kolude Experimental Equipment Co., Ltd., China. Polypropylene (PP) membrane was obtained from Shanghai Xingya Purification Materials Factory Co., Ltd., China. Potassium chloride (KCl, AR, ≥99.8%), sodium chloride (NaCl, AR, ≥99.8%), sodium sulfate ($NaSO_4$, AR, ≥99.8%) and phosphoric acid (H_3PO_4, AR, ≥99.8%) were purchased from Sinopharm Chemical Reagent Co., Ltd., China. Phenol (C_6H_6O, ≥99%), sulfamethazine ($C_{12}H_{14}N_4O_2S$, 98%), tetracycline hydrochloride ($C_{22}H_{24}N_2O_8$•HCl, 96%), ciprofloxacin ($C_{17}H_{18}FN_3O_3$, 98%), and enrofloxacin ($C_{19}H_{22}FN_3O_3$, 98%) were obtained from Shanghai Aladdin Biochemical Technology Co., Ltd., China. Formic acid (CH_2O_2, HPLC, ≥99%) and methanol (CH_4O, HPLC grade) were purchased from Shanghai Macklin Biochemical Co., Ltd., China and Sigma-Aldrich, respectively. All aqueous solutions were prepared using ultrapure water from a Milli-Q system.

Electrochemical measurement

All electrochemical experiments were conducted at room temperature using a Bio-Logic SP-300 workstation. Carbon felt electrodes (10 mm × 20 mm × 3 mm) served as both the working and counter electrodes, separated by a polypropylene (PP) membrane with 110 μm thickness and 92% porosity. Titanium mesh and titanium foil were used as current collectors, and an Ag/AgCl electrode served as the reference electrode. Experiments were performed in a custom-made flow-through electrode system, with solution supplied either by peristaltic pump. Electrochemical impedance spectroscopy (EIS) measurements were performed under open-circuit conditions with a 10 mV perturbation, or under an applied cell voltage of 3 V (DRT related test), over a frequency range of 10 mHz-1 MHz, scanning from high to low frequency. Data points were recorded at ten points per decade of frequency. For five-channel method, two electrochemical workstations (EC-1, EC-2) were operated simultaneously: EC-1 applied cell voltage to the electrolysis cell, while EC-2 monitored the electrode

potentials. Controlled experiment of single-chamber cell and linear sweep voltammetry (LSV) scans were performed in 50 mL single-chamber cells without compartmentalization. And experiments of H-cell (50 mL per compartment) were separated by a Nafion 117 membrane and each filled with 40 mL of electrolyte.

Analytical Methods.

The maximum absorbance wavelengths of the target organic chemicals were determined using a Shimadzu UV-Vis spectrophotometer (UV-2600i, Shimadzu, Japan). The maximum absorbance wavelengths for phenol, sulfamethazine (SDZ), tetracycline (TC), ciprofloxacin (CIP), and enrofloxacin (ENR) were 270 nm, 265 nm, 356 nm, 277 nm, and 277 nm, respectively, and were used for subsequent quantitative analysis by liquid chromatography.

Phenol and phenol derivative concentrations and partial product concentrations were measured using a high-performance liquid chromatography (HPLC) system (Agilent 1260) equipped with a diode-array detector (DAD) and a C18 reversed-phase column (5 μm, 4.6 mm × 150 mm). For phenol and its products, the mobile phase ratio was methanol: water (0.02% formic acid) = 60: 40 (v/v), with a flow rate of 1 mL min^{-1}, column temperature of 25 ℃, and injection volume of 10 μL. For antibiotic analysis, the mobile phase ratio was methanol: water (0.02% formic acid) = 70: 30 (v/v), with all other conditions unchanged.

Prior to analysis of small-molecule products, samples were passed through a silver ion-exchange column to remove Cl^- interference, followed by quantitative determination using an ion chromatography (IC) system (Themo Scientific Dionex) equipped with a Dionex IonPac AS11-HC RFIC (4 mm × 250 mm). A gradient elution was applied: 1 mmol L^{-1} KOH for the first 14 min, ramped to 10 mmol L^{-1} within 0.1 min, and held for an additional 14 min. Total organic carbon (TOC) was measured using a Shimadzu TOC analyzer (TOC-L, Shimadzu, Japan). All samples were filtered through a 0.22 μm membrane prior to injection.

Operando electrochemical Raman spectroscopy

Au@SiO_2 nanoparticles (with a 55 nm Au core and a 2 nm SiO_2 shell) were purchased from Xiamen Cynan Technology Co., Ltd., China. Prior to use, the

nanoparticles were cleaned according to a previously established method and diluted to 0.1 g L^{-1}[56]. A suitable aliquot of this dispersion was uniformly drop-cast onto a graphite electrode (10 mm × 20 mm) and dried under a gentle Ar stream. The electrode was deemed suitable when SEM characterization confirmed an Au@SiO_2 surface coverage of 10-25% (Supplementary Fig. 39). The as-prepared surface-enhanced electrode was then employed as both the working and counter electrode and assembled into a custom-made Raman electrochemical cell (Supplementary Fig. 40). The two-electrode system was placed horizontally, and the objective lens illuminated the testing electrode vertically. The alternating current (3 V, 0.01 Hz, Square Wave) was applied to the two-electrode system, and Raman spectra were obtained during the reaction. During testing, the electrolyte consisting of 100 mg L^{-1} phenol and 0.1 mol L^{-1} KCl was continuously circulated through the system at a flow rate of 1 mL min^{-1}. Electrochemical in situ Raman spectra were tested with inVia^{TM} confocal Raman microscope (Renishaw, UK) with 785 nm laser，10% Laser power，50× objective lens，10s exposure time. A standard silicon wafer of 520.5 cm^{-1} was used for calibration before each test.

EIS Data Validation and DRT Analysis

The validity of electrochemical impedance spectroscopy (EIS) measurements was assessed using Kramers-Kronig analysis implemented in Nova 2.0.1 software. EIS data were considered valid when the sum of squared residuals between the real and imaginary components of impedance was below 10^{-4} (Supplementary Table 4).

For valid EIS datasets, the distribution of relaxation times (DRT) was calculated using the open-source MATLAB script DRT Tools[57], employing the Tikhonov regularization method for nonlinear least-squares fitting of discrete experimental data. Data discretization was performed using Gaussian functions. Only the real and imaginary components of the EIS spectra were used for fitting; inductive contributions were excluded. A second-order derivative regularization was applied with a regularization parameter of 0.0001. Radial basis functions (RBF) were used for the discretization with a full width at half maximum (FWHM) of 0.5, which provided an appropriate fit to the EIS data[58].

Computational methods

Molecular dynamics simulation. Molecular dynamics simulations (MD) were

performed using the Large-Scale Atomic/Molecular Massively Parallel Simulator (LAMMPS) package. The model applies periodic boundary conditions parallel to the electrode electrolyte interface direction. During the simulation process, the electrode atoms are fixed in position and react with the electrolyte through charge transfer. The initial temperature of 298 K and NVT (constant number of atoms N, volume V, and temperature T) ensemble constraints are applied during the simulation process. The total duration of the simulation is set at 1 ns, with a timestep of 2 fs. Atomistic trajectory data is recorded every 0.2 ps and averaged over 50 configurations at specific time points to ensure data reliability and facilitate further analysis. A voltage is applied from an electrode to another electrode to replicate electrolysis operation. The kalium or carbon atoms at the electrodes are fixed while allowing charge exchange with the electrolyte[59].

Quantum chemistry calculations. To obtain insights into the greater detail from the perspective of charge distribution, density functional theory (DFT) calculations were conducted to examine the surface transformation under different potentials. The total and partial density of states (DOS) for each element (Fig. 5c) are computed using the DFT method. The atomic configurations were analyzed by using open visualization tool software (OVITO). Reaction energy barriers for the phenol mineralization process (Supplementary Fig. 42) were calculated using DFT. All molecular structures were constructed in Gaussian software. Geometry optimizations and molecular energy calculations were performed at the B3LYP/6-311+G (d, p) level of theory. The reaction energy barrier for each step was obtained as the difference between the molecular energies of the products and the corresponding reactants.

Data availability

The data that support the findings of this study have been included in the main text and the Supplementary Information.

Acknowledgements

This research was supported by the National Key Research and Development Program of China (2024YFC3713303), the National Natural Science Foundations of China (22406167, 22576178), the Zhejiang Provincial Natural Science Foundation of China (LZ24B070001), and the Provincial “Leading Goose” Key Technology Research and Development Program of Zhejiang, China (2023C03139, 2024C03125).

Author contributions

X.X., W.Y. and B.C. supervised the project. H.Z. and X.X. conceived the idea and designed the experiments. H.Z. carried out the experiments and wrote the paper. Z.W. performed the COMSOL simulations. C.G. helped with the theory calculations. Y.L. and H.L participated in the design and discussion of some experiments.

Competing interests

The authors declare no competing interests.

Supplementary Files

This is a list of supplementary files associated with this preprint. Click to download.

- Supportinginformation.pdf